

# The 2dF Galaxy Redshift Survey: Wiener Reconstruction of the Cosmic Web

Pirin Erdoğdu<sup>1,2</sup>, Ofer Lahav<sup>1</sup>, Saleem Zaroubi<sup>3</sup>, George Efstathiou<sup>1</sup>, Steve Moody, John A. Peacock<sup>12</sup>, Matthew Colless<sup>17</sup>, Ivan K. Baldry<sup>9</sup>, Carlton M. Baugh<sup>16</sup>, Joss Bland-Hawthorn<sup>7</sup>, Terry Bridges<sup>7</sup>, Russell Cannon<sup>7</sup>, Shaun Cole<sup>16</sup>, Chris Collins<sup>4</sup>, Warrick Couch<sup>5</sup>, Gavin Dalton<sup>6,15</sup>, Roberto De Propris<sup>17</sup>, Simon P. Driver<sup>17</sup>, Richard S. Ellis<sup>8</sup>, Carlos S. Frenk<sup>16</sup>, Karl Glazebrook<sup>9</sup>, Carole Jackson<sup>17</sup>, Ian Lewis<sup>6</sup>, Stuart Lumsden<sup>10</sup>, Steve Maddox<sup>11</sup>, Darren Madgwick<sup>13</sup>, Peder Norberg<sup>14</sup>, Bruce A. Peterson<sup>17</sup>, Will Sutherland<sup>12</sup>, Keith Taylor<sup>8</sup> (The 2dFGRS Team)

<sup>1</sup>*Institute of Astronomy, Madingley Road, Cambridge CB3 0HA, UK*

<sup>2</sup>*Department of Physics, Middle East Technical University, 06531, Ankara, Turkey*

<sup>3</sup>*Max Planck Institut für Astrophysik, Karl-Schwarzschild-Straße 1, 85741 Garching, Germany*

<sup>4</sup>*Astrophysics Research Institute, Liverpool John Moores University, Twelve Quays House, Birkenhead, L14 1LD, UK*

<sup>5</sup>*Department of Astrophysics, University of New South Wales, Sydney, NSW 2052, Australia*

<sup>6</sup>*Department of Physics, University of Oxford, Keble Road, Oxford OX1 3RH, UK*

<sup>7</sup>*Anglo-Australian Observatory, P.O. Box 296, Epping, NSW 2111, Australia*

<sup>8</sup>*Department of Astronomy, California Institute of Technology, Pasadena, CA 91025, USA*

<sup>9</sup>*Department of Physics & Astronomy, Johns Hopkins University, Baltimore, MD 21118-2686, USA*

<sup>10</sup>*Department of Physics, University of Leeds, Woodhouse Lane, Leeds, LS2 9JT, UK*

<sup>11</sup>*School of Physics & Astronomy, University of Nottingham, Nottingham NG7 2RD, UK*

<sup>12</sup>*Institute for Astronomy, University of Edinburgh, Royal Observatory, Blackford Hill, Edinburgh EH9 3HJ, UK*

<sup>13</sup>*Lawrence Berkeley National Laboratory, 1 Cyclotron Road, Berkeley, CA 94720, USA*

<sup>14</sup>*ETHZ Institut für Astronomie, HPF G3.1, ETH Hönggerberg, CH-8093 Zurich, Switzerland*

<sup>15</sup>*Rutherford Appleton Laboratory, Chilton, Didcot, OX11 0QX, UK*

<sup>16</sup>*Department of Physics, University of Durham, South Road, Durham DH1 3LE, UK*

<sup>17</sup>*Research School of Astronomy & Astrophysics, The Australian National University, Weston Creek, ACT 2611, Australia*

9 November 2018

## ABSTRACT

We reconstruct the underlying density field of the 2 degree Field Galaxy Redshift Survey (2dFGRS) for the redshift range  $0.035 < z < 0.200$  using the Wiener Filtering method. The Wiener Filter suppresses shot noise and accounts for selection and incompleteness effects. The method relies on prior knowledge of the 2dF power spectrum of fluctuations and the combination of matter density and bias parameters however the results are only slightly affected by changes to these parameters. We present maps of the density field in two different resolutions:  $5h^{-1}$  Mpc and  $10h^{-1}$  Mpc. We identify all major superclusters and voids in the survey. In particular, we find two large superclusters and two large local voids. A version of this paper with full set of colour maps can be found at <http://www.ast.cam.ac.uk/~pirin>.

**Key words:** galaxies:distances and redshifts - cosmology: large-scale structure of Universe - methods: statistical

## 1 INTRODUCTION

Historically, redshift surveys have provided the data and the test ground for much of the research on the nature of clustering and the distribution of galaxies. In the past few years, observations of large scale structure have improved greatly. Today, with the development of fibre-fed spectrographs that can simultaneously measure spectra

of hundreds of galaxies, cosmologists have at their fingertips large redshift surveys such as 2 degree Field (2dF) and Sloan Digital Sky Survey (SDSS). The analysis of these redshift surveys yield invaluable cosmological information. On the quantitative side, with the assumption that the galaxy distribution arises from the gravitational instability of small fluctuations generated in the early universe, a

wide range of statistical measurements can be obtained, such as the power spectrum and bispectrum. Furthermore, a qualitative understanding of galaxy distribution provides insight into the mechanisms of structure formation that generate the complex pattern of sheets and filaments comprising the ‘cosmic web’ (Bond, Kofman & Pogosyan 1996) we observe and allows us to map a wide variety of structure, including clusters, superclusters and voids.

Today, many more redshifts are available for galaxies than direct distance measurements. This discrepancy inspired a great deal of work on methods for reconstruction of the real-space density field from that observed in redshift-space. These methods use a variety of functional representations (e.g. Cartesian, Fourier, spherical harmonics or wavelets) and smoothing techniques (e.g. a Gaussian sphere or a Wiener Filter). There are physical as well as practical reasons why one would be interested in smoothing the observed density field. It is often assumed that the galaxy distribution samples the underlying smooth density field and the two are related by a proportionality constant, the so-called linear bias parameter,  $b$ . The finite sampling of the smooth underlying field introduces Poisson ‘shot noise’<sup>1</sup>. Any robust reconstruction technique must reliably mitigate the statistical uncertainties due to shot noise. Moreover, in redshift surveys, the actual number of galaxies in a given volume is larger than the number observed, in particular in magnitude limited samples where at large distances only very luminous galaxies can be seen.

In this paper, we analyse large scale structure in the 2 degree Field Galaxy Redshift Survey (2dFGRS, Colless *et al.* 2001), which has now obtained the redshifts for approximately 230,000 galaxies. We recover the underlying density field, characterised by an assumed power spectrum of fluctuations, from the observed field which suffers from incomplete sky coverage (described by the angular mask) and incomplete galaxy sampling due to its magnitude limit (described by the selection function). The filtering is achieved by a Wiener Filter (Wiener 1949, Press *et al.* 1992) within the framework of both linear and non-linear theory of density fluctuations. The Wiener Filter is optimal in the sense that the variance between the derived reconstruction and the underlying true density field is minimised. As opposed to *ad hoc* smoothing schemes, the smoothing due to the Wiener Filter is determined by the data. In the limit of high signal-to-noise, the Wiener Filter modifies the observed data only weakly, whereas it suppresses the contribution of the data contaminated by shot noise.

The Wiener Filtering is a well known technique and has been applied to many fields in astronomy (see Rybicki & Press 1992). For example, the method was used to reconstruct the angular distribution (Lahav *et al.* 1994), the real-space density, velocity and gravitational potential fields of the 1.2 Jy-*IRAS* (Fisher *et al.* 1995) and *IRAS* PSCz surveys (Schmoldt *et al.* 1999). The Wiener Filter was also applied to the reconstruction of the angular maps of the Cosmic Microwave Background temperature fluctuations (Bunn *et al.* 1994, Tegmark & Efstathiou 1995, Bouchet & Gispert 1999). A detailed formalism of the Wiener Filtering method as it pertains to the large scale structure reconstruction can be found in Zaroubi *et al.* (1995).

This paper is structured as follows: we begin with a brief review of the formalism of the Wiener Filter method. A summary

<sup>1</sup> Another popular model for galaxy clustering is the halo model where the linear bias parameter depends on the mass of the dark matter halos where the galaxies reside. For this model, the mean number of galaxy pairs in a given halo is usually lower than the Poisson expectation.

of 2dFGRS data set, the survey mask and the selection function are given in Section 3. In section 4, we outline the scheme used to pixelise the survey. In section 5, we give the formalism for the covariance matrix used in the analysis. After that, we describe the application of the Wiener Filter method to 2dFGRS and present detailed maps of the reconstructed field. In section 7, we identify the superclusters and voids in the survey.

Throughout this paper, we assume a  $\Lambda$ CDM cosmology with  $\Omega_m = 0.3$  and  $\Omega_\Lambda = 0.7$  and  $H_0 = 100h^{-1} \text{ km s}^{-1} \text{ Mpc}^{-1}$ .

## 2 WIENER FILTER

In this section, we give a brief description of the Wiener Filter method. For more details, we refer the reader to Zaroubi *et al.* (1995). Let’s assume that we have a set of measurements,  $\{d_\alpha\}$  ( $\alpha = 1, 2, \dots, N$ ) which are a linear convolution of the true underlying signal,  $s_\alpha$ , plus a contribution from statistical noise,  $\epsilon_\alpha$ , such that

$$d_\alpha = s_\alpha + \epsilon_\alpha. \quad (1)$$

The Wiener Filter is defined as the *linear* combination of the observed data which is closest to the true signal in a minimum variance sense. More explicitly, the Wiener Filter estimate,  $s_\alpha^{WF}$ , is given by  $s_\alpha^{WF} = F_{\alpha\beta} d_\beta$  where the filter is chosen to minimise the variance of the residual field,  $r_\alpha$ :

$$\langle |r_\alpha|^2 \rangle = \langle |s_\alpha^{WF} - s_\alpha|^2 \rangle. \quad (2)$$

It is straightforward to show that the Wiener Filter is given by

$$F_{\alpha\beta} = \langle s_\alpha d_\gamma^\dagger \rangle \langle d_\gamma d_\beta^\dagger \rangle^{-1}, \quad (3)$$

where the first term on the right hand side is the signal-data correlation matrix;

$$\langle s_\alpha d_\gamma^\dagger \rangle = \langle s_\alpha s_\gamma^\dagger \rangle, \quad (4)$$

and the second term is the data-data correlation matrix;

$$\langle d_\alpha d_\beta^\dagger \rangle = \langle s_\gamma s_\delta^\dagger \rangle + \langle \epsilon_\alpha \epsilon_\beta^\dagger \rangle. \quad (5)$$

In the above equations, we have assumed that the signal and noise are uncorrelated. From equations 3 and 5, it is clear that, in order to implement the Wiener Filter, one must construct a *prior* which depends on the mean of the signal (which is 0 by construction) and the variance of the signal and noise. The assumption of a prior may be alarming at first glance. However, slightly inaccurate values of Wiener Filter will only introduce second order errors to the full reconstruction (see Rybicki & Press 1992). The dependence of the Wiener Filter on the prior can be made clear by defining signal and noise matrices as  $C_{\alpha\beta} = \langle s_\alpha s_\beta^\dagger \rangle$  and  $N_{\alpha\beta} = \langle \epsilon_\alpha \epsilon_\beta^\dagger \rangle$ . With this notation, we can rewrite the equations above so that  $s^{WF}$  is given as

$$s^{WF} = \mathbf{C} [\mathbf{C} + \mathbf{N}]^{-1} \mathbf{d}. \quad (6)$$

The mean square residual given in equation 2 can then be calculated as

$$\langle \mathbf{r} \mathbf{r}^\dagger \rangle = \mathbf{C} [\mathbf{C} + \mathbf{N}]^{-1} \mathbf{N}. \quad (7)$$

Formulated in this way, we see that the purpose of the Wiener Filter is to attenuate the contribution of low signal-to-noise ratio data. The derivation of the Wiener Filter given above follows from the sole requirement of minimum variance and requires only a model for the variance of the signal and noise. The Wiener Filter can also be derived using the laws of conditional probability if

the underlying distribution functions for the signal and noise are assumed to be Gaussian. For the Gaussian prior, the Wiener Filter estimate is both the maximum *posterior* estimate and the mean field (see Zaroubi *et al.* 1995).

As several authors point out (e.g. Rybicki & Press 1992, Zaroubi 2002), the Wiener Filter is a biased estimator since it predicts a null field in the absence of good data, unless the field itself has zero mean. Since we constructed the density field to have zero mean, we are not worried about this bias. However, the observed field deviates from zero due to selection effects and so one needs to be aware of this bias in the reconstructions.

It is well known that the peculiar velocities of galaxies distort clustering pattern in redshift space. On small scales, the random peculiar velocity of each galaxy causes smearing along the line of sight, known as *the finger of God*. On larger scales, there is compression of structures along the line of sight due to coherent infall velocities of large-scale structure induced by gravity. One of the major difficulties in analysing redshift surveys is the transformation of the position of galaxies from redshift space to real space. For all sky surveys, this issue can be addressed using several methods, for example the iterative method of Yahil *et al.* (1991) and modified Poisson equation of Nusser & Davis 1994. However, these methods are not applicable to surveys which are not all sky as they assume that in linear theory, the peculiar velocity of any galaxy is a result of the matter distribution around it, and the gravitational field is dominated by the matter distribution inside the volume of the survey. For a survey like 2dFGRS, within the limitation of linear theory where the redshift space density is a linear transformation of the real space density, a Wiener Filter can be used to transform from redshift space to real space (see Fisher *et al.* (1995) and Zaroubi *et al.* (1995) for further details). This can be written as

$$s^{WF}(r_\alpha) = \langle s(r_\alpha)d(s_\gamma) \rangle \langle d(s_\gamma)d(s_\beta) \rangle^{-1} d(s_\beta), \quad (8)$$

where the first term on the right hand side is the cross-correlation matrix of real and redshift space densities and  $\mathbf{s}(\mathbf{r})$  is the position vector in redshift space. It is worth emphasising that this method is limited as it only recovers the peculiar velocity field generated by the mass sources represented by the galaxies within the survey boundaries. It does not account for possible external forces. This limitation can only be overcome by comparing the 2dF survey with all sky surveys.

### 3 THE DATA

#### 3.1 The 2dFGRS data

The 2dFGRS, now completed, is selected in the photometric  $b_J$  band from the APM galaxy survey (Maddox, Efstathiou & Sutherland 1990) and its subsequent extensions (Maddox *et al.* 2003, in preparation). The survey covers about 2000 deg<sup>2</sup> and is made up of two declination strips, one in the South Galactic Pole region (SGP) covering approximately  $-37^\circ.5 < \delta < -22^\circ.5$ ,  $-35^\circ.0 < \alpha < 55^\circ.0$  and the other in the direction of the North Galactic Pole (NGP), spanning  $-7^\circ.5 < \delta < 2^\circ.5$ ,  $147^\circ.5 < \alpha < 222^\circ.5$ . In addition to these contiguous regions, there are a number of randomly located circular 2-degree fields scattered over the full extent of the low extinction regions of the southern APM galaxy survey.

The magnitude limit at the start of the survey was set at  $b_J = 19.45$  but both the photometry of the input catalogue and the dust extinction map have been revised since and so there are small variations in magnitude limit as a function of position over the sky

which are taken into account using the magnitude limit mask. The effective median magnitude limit, over the area of the survey, is  $b_J \approx 19.3$  (Colless *et al.* 2001).

We use the data obtained prior to May 2002, when the survey was nearly complete. This includes 221 283 unique, reliable galaxy redshifts. We analyse a magnitude-limited sample with redshift limits  $z_{\min} = 0.035$  and  $z_{\max} = 0.20$ . The median redshift is  $z_{\text{med}} \approx 0.11$ . We use 167 305 galaxies in total, 98 129 in the SGP and 69 176 in the NGP. We do not include the random fields in our analysis.

The 2dFGRS database and full documentation are available on the WWW at <http://www.mso.anu.edu.au/2dFGRS/>.

#### 3.2 The Mask and The Radial Selection Function of 2dFGRS

The completeness of the survey varies according to the position in the sky due to unobserved fields, particularly at the survey edges, and unfibred objects in the observed fields because of collision constraints or broken fibres.

For our analysis, we make use of two different masks (Colless *et al.* 2001; Norberg *et al.* 2002). The first of these masks is the redshift completeness mask defined as the ratio of the number of galaxies for which redshifts have been measured to the total number of objects in the parent catalogue. This spatial incompleteness is illustrated in Figure 1. The second mask is the magnitude limit mask which gives the extinction corrected magnitude limit of the survey at each position.

The radial selection function gives the probability of observing a galaxy for a given redshift and can be readily calculated from the galaxy luminosity function:

$$\Phi(L)dL = \Phi^* \left( \frac{L}{L_*} \right)^\alpha \exp \left( -\frac{L}{L_*} \right) \frac{dL}{L_*}. \quad (9)$$

where for the concordance model:  $\alpha = -1.21 \pm 0.03$ ,  $\log_{10} L_* = -0.4(-19.66 \pm 0.07 + 5 \log_{10}(h))$  and  $\Phi_* = 0.0161 \pm 0.0008 h^3$  (Norberg *et al.* 2002).

The selection function can then be expressed as

$$\phi(r) = \frac{\int_{L(r)}^{\infty} \Phi(L)dL}{\int_{L_{\min}}^{\infty} \Phi(L)dL}, \quad (10)$$

where  $L(r)$  is the minimum luminosity detectable at luminosity distance  $r$  (assuming the concordance model), evaluated for the concordance model,  $L_{\min} = \text{Min}(L(r), L_{\text{com}})$  and  $L_{\text{com}}$  is the minimum luminosity for which the catalogue is complete and varies as a function of position over the sky. For distances considered in this paper, where the deviations from the Hubble flow are relatively small, the selection function can be approximated as  $\phi(r) \approx \phi(z_{\text{gal}})$ . Each galaxy, *gal*, is then assigned the weight

$$w(\text{gal}) = \frac{1}{\phi(z_{\text{gal}})M(\Omega_i)} \quad (11)$$

where  $\phi(z_{\text{gal}})$  and  $M(\Omega_i)$  are the values of the selection function for each galaxy and angular survey mask for each cell  $i$  (see Section 4), respectively.

### 4 SURVEY PIXELISATION

In order to form a data vector of overdensities, the survey needs to be pixelised. There are many ways to pixelise a survey: equal sized cubes in redshift space, igloo cells, spherical harmonics, Delaunay tessellation methods, wavelet decomposition, etc. Each of

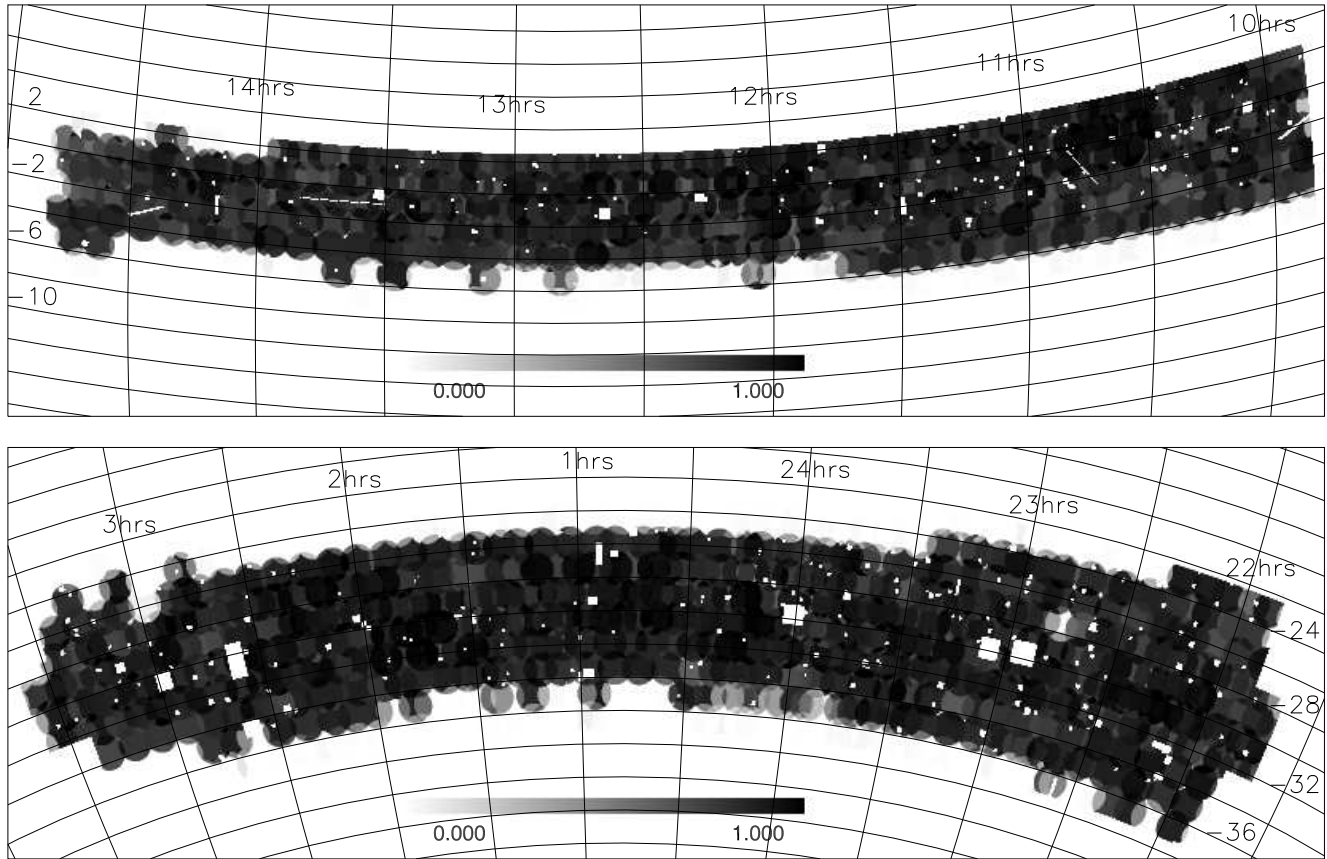


**Figure 1.** The redshift completeness masks for the NGP (top) and SGP (bottom) in Equatorial coordinates. The gray scale shows the completeness fraction.

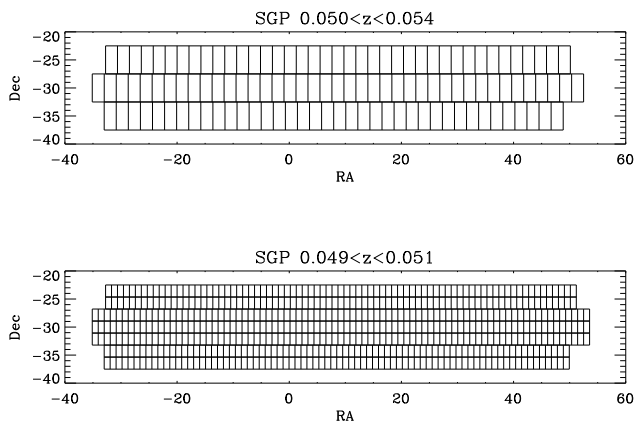


**Figure 2.** An illustration of the survey pixelisation scheme used in the analysis, for  $10h^{-1}$  Mpc (top) and  $5h^{-1}$  Mpc (bottom) target cells widths. The redshift ranges given on top of each plot.

these methods have their own advantages and disadvantages and they should be treated with care as they form functional bases in which all the statistical and physical properties of cosmic fields are retained.

The pixelisation scheme used in this analysis is an ‘igloo’ grid with wedge shaped pixels bounded in right ascension, declination

and in redshift. The pixelisation is constructed to keep the average number density per pixel approximately constant. The advantage of using this pixelisation is that the number of pixels is minimised since the pixel volume is increased with redshift to counteract the decrease in the selection function. This is achieved by selecting a ‘target cell width’ for cells at the mean redshift of the survey and deriving the rest of the bin widths so as to match the shape of the selection function. The target cell widths used in this analysis are  $10h^{-1}$  Mpc and  $5h^{-1}$  Mpc. Once the redshift binning has been calculated each radial bin is split into declination bands and then each band in declination is further divided into cells in right ascension. The process is designed so as to make the cells roughly cubical. In Figure 2, we show an illustration of this by plotting the cells in right ascension and declination for a given redshift strip.

Although advantageous in many ways, the pixelisation scheme used in this paper may complicate the interpretation of the reconstructed field. By definition, the Wiener Filter signal will approach to zero at the edges of the survey where the shot noise may dominate. This means the true signal will be constructed in a non-uniform manner. This effect will be amplified as the cell sizes get bigger at higher redshifts. Hence, both of these effects must be considered when interpreting the results.

## 5 ESTIMATING THE SIGNAL-SIGNAL CORRELATION MATRIX OVER PIXELS

The signal covariance matrix can be accurately modelled by an analytical approximation (Moody 2003). The calculation of the covariance matrix is similar to the analysis described by Efstathiou and Moody (2001) apart from the modification due to three-dimensionality of the survey. The covariance matrix for the ‘noise free’ density fluctuations is  $\langle C_{ij} \rangle = \langle \delta_i \delta_j \rangle$ , where  $\delta_i = (\rho_i - \bar{\rho})/\bar{\rho}$  in the  $i$ th pixel. It is estimated by first considering a pair of pixels with volumes  $V_i$  and  $V_j$ , separated by distance  $\mathbf{r}$  so that,

$$\langle C_{ij} \rangle = \left\langle \frac{1}{V_i V_j} \int_{Cell_i} \delta(\mathbf{x}) dV_i \int_{Cell_j} \delta(\mathbf{x} + \mathbf{r}) dV_j \right\rangle \quad (12)$$

$$= \frac{1}{V_i V_j} \int_{Cell_i} \int_{Cell_j} \langle \delta(\mathbf{x}) \delta(\mathbf{x} + \mathbf{r}) \rangle dV_i dV_j \quad (13)$$

$$= \frac{1}{V_i V_j} \int_{Cell_i} \int_{Cell_j} \xi(\mathbf{r}) dV_i dV_j \quad (14)$$

where the isotropic two point correlation function  $\xi(r)$  is given by

$$\xi(r) = \frac{1}{(2\pi)^3} \int P(k) e^{-i\mathbf{k}\cdot\mathbf{r}} d^3k, \quad (15)$$

and therefore,

$$\langle C_{ij} \rangle = \frac{1}{(2\pi)^3 V_i V_j} \int P(k) d^3k \times \int_{Cell_i} \int_{Cell_j} e^{-i\mathbf{k}(\mathbf{r}_i - \mathbf{r}_j)} dV_i dV_j. \quad (16)$$

After performing the Fourier transform, this equation can be written as

$$\langle C_{ij} \rangle = \frac{1}{(2\pi)^3} \int P(k) S(\mathbf{k}, \mathbf{L}_i) S(\mathbf{k}, \mathbf{L}_j) C(\mathbf{k}, \mathbf{r}) d^3k, \quad (17)$$

where the functions  $S$  and  $C$  are given by,

$$S(\mathbf{k}, \mathbf{L}) = \text{sinc}(k_x L_x / 2) \text{sinc}(k_y L_y / 2) \text{sinc}(k_z L_z / 2) \quad (18)$$

$$C(\mathbf{k}, \mathbf{r}) = \cos(k_x r_x) \cos(k_y r_y) \cos(k_z r_z), \quad (19)$$

where the label  $\mathbf{L}$  describes the dimensions of the cell ( $L_x$ ,  $L_y$ ,  $L_z$ ), the components of  $\mathbf{r}$  describes the separation between cell centres,  $\mathbf{k} = (k_x, k_y, k_z)$  is the wavevector and  $\text{sinc}(x) = \frac{\sin(x)}{x}$ . The wavevector,  $\mathbf{k}$  is written in spherical co-ordinates  $k$ ,  $\theta$ ,  $\phi$  to simplify the evaluation of  $C$ . We define,

$$k_x = k \sin(\phi) \cos(\theta) \quad (20)$$

$$k_y = k \sin(\phi) \sin(\theta) \quad (21)$$

$$k_z = k \cos(\phi). \quad (22)$$

Equation 17 can now be integrated over  $\theta$  and  $\phi$  to form the kernel  $G_{ij}(k)$  where,

$$G_{ij}(k) = \frac{1}{\pi^3} \int_0^{\pi/2} \int_0^{\pi/2} S(\mathbf{k}, \mathbf{L}_i) S(\mathbf{k}, \mathbf{L}_j) C(\mathbf{k}, \mathbf{r}) \sin(\phi) d\theta d\phi, \quad (23)$$

so that,

$$\langle C_{ij} \rangle = \int P(k) G_{ij}(k) k^2 dk. \quad (24)$$

In practice we evaluate,

$$\langle C_{ij} \rangle = \sum_k P_k G_{ijk}, \quad (25)$$

where  $P_k$  is the binned bandpower spectrum and  $G_{ijk}$  is,

$$G_{ijk} = \int_{k_{min}}^{k_{max}} G_{ij}(k) k^2 dk, \quad (26)$$

where the integral extends over the band corresponding to the band power  $P_k$ .

For cells that are separated by a distance much larger than the cell dimensions the cell window functions can be ignored, simplifying the calculation so that,

$$G_{ijk} = \frac{1}{(2\pi)^3} \int_{k_{min}}^{k_{max}} \text{sinc}(kr) 4\pi k^2 dk, \quad (27)$$

where  $r$  is the separation between cell centres.

## 6 THE APPLICATION

### 6.1 Reconstruction Using Linear Theory

In order to calculate the data vector  $\mathbf{d}$  in equation 6, we first estimate the number of galaxies  $N_i$  in each pixel  $i$ :

$$N_i = \sum_{gal}^{N_{gal}(i)} w(gal), \quad (28)$$

where the sum is over all the observed galaxies in the pixel and  $w(gal)$  is the weight assigned to each galaxy (equation 11). The boundaries of each pixel are defined by the scheme described in Section 4, using a target cell width of  $10h^{-1}$  Mpc. The mean number of galaxies in pixel  $i$  is

$$\bar{N}_i = \bar{n} V_i, \quad (29)$$

where  $V_i$  is the volume of the pixel and the mean galaxy density,  $\bar{n}$ , is estimated using the equation:

$$\bar{n} = \frac{\sum_{gal}^{N_{total}} w(gal)}{\int_0^\infty dr r^2 \phi(r) w(r)}, \quad (30)$$

where the sum is now over all the galaxies in the survey. We note that the value for  $\bar{n}$  obtained using the equation above is consistent with the maximum estimator method proposed by Davis and Huchra (1982). Using these definitions, we write the  $i$ th component of the data vector  $\mathbf{d}$  as:

$$d_i = \frac{N_i - \bar{N}_i}{\bar{N}_i}. \quad (31)$$

Note that, the mean value of  $\mathbf{d}$  is zero by construction.

Reconstruction of the underlying signal given in equation 6 also requires the signal-signal and the inverse of the data-data correlation matrices. The data-data correlation matrix (equation 5) is the sum of noise-noise correlation matrix  $\mathbf{N}$  and the signal-signal correlation matrix  $\mathbf{C}$  formulated in the previous section. The only change made is to the calculation of  $\mathbf{C}$  where the real space correlation function  $\xi(r)$  is now multiplied by Kaiser’s factor in order to correct for the redshift distortions on large scales. So

$$\xi_s = \frac{1}{(2\pi)^3} \int P^S(k) \exp(i\mathbf{k} \cdot (\mathbf{r}_2 - \mathbf{r}_1)) d^3k, \quad (32)$$

where  $P^S(k)$  is the galaxy power spectrum in redshift space,

$$P^S(k) = K[\beta]P^R(k), \quad (33)$$

derived in linear theory. The subscripts  $R$  and  $S$  in this equation (and hereafter) denote real and redshift space, respectively.

$$K[\beta] = 1 + \frac{2}{3}\beta + \frac{1}{5}\beta^2 \quad (34)$$

is the direction averaged Kaiser's (1987) factor, derived using distant observer approximation and with the assumption that the data subtends a small solid angle with respect to the observer (the latter assumption is valid for the 2dFGRS but does not hold for a wide angle survey, see Zaroubi and Hoffman, 1996 for a full discussion). Equation 33 shows that in order to apply the Wiener Filter method, we need a model for the galaxy power spectrum in redshift-space which depends on the real-space power spectrum spectrum and on the redshift distortion parameter,  $\beta \equiv \Omega_m^{0.6}/b$ .

The real-space galaxy power spectrum is well described by a scale invariant Cold Dark Matter power spectrum with shape parameter,  $\Gamma$  for the scales concerned in this analysis. For  $\Gamma$ , we use the value derived from the 2dF survey by Percival *et al.* (2001) who fitted the 2dFGRS power spectrum over the range of linear scales using the fitting formulae of Eisenstein and Hu (1998). Assuming a Gaussian prior on the Hubble constant  $h = 0.7 \pm 0.07$  (based on Freedman *et al.* 2001), they find  $\Gamma = 0.2 \pm 0.03$ . The normalisation of the power spectrum is conventionally expressed in terms of the variance of the density field in spheres of  $8h^{-1}$  Mpc,  $\sigma_8$ . Lahav *et al.* (2002) use 2dFGRS data to deduce  $\sigma_{8g}^S(L_s, z_s) = 0.94 \pm 0.02$  for the galaxies in redshift space, assuming  $h = 0.7 \pm 0.07$  at  $z_s \approx 0.17$  and  $L_s \approx 1.9L^*$ . We convert this result to real space using the following equation:

$$\sigma_{8g}^R(L_s, z_s) = \sigma_{8g}^S(L_s, z_s)/K^{1/2}[\beta(L_s, z_s)]. \quad (35)$$

where  $K[\beta]$  is Kaiser's factor. For our analysis, we need to use  $\sigma_8$  evaluated at the mean redshift of the survey for galaxies with luminosity  $L^*$ . However, one needs to assume a model for the evolution of galaxy clustering in order to find  $\sigma_8$  at different redshifts. Moreover, the conversion from  $L_s$  to  $L^*$  introduces uncertainties in the calculation. Therefore, we choose an approximate value,  $\sigma_{8g}^R \approx 0.8$  to normalise the power spectrum. For  $\beta$ , we adopt the value found by Hawkins *et al.* (2002),  $\beta(L_s, z_s) = 0.49 \pm 0.09$  which is estimated at the effective luminosity,  $L_s \approx 1.4L^*$ , and the effective redshift,  $z_s \approx 0.15$ , of the survey sample. Our results are not sensitive to minor changes in  $\sigma_8$  and  $\beta$ .

The other component of the data-data correlation matrix is the noise correlation matrix  $\mathbf{N}$ . Assuming that the noise in different cells is not correlated, the only non-zero terms in  $\mathbf{N}$  are the diagonal terms given by the variance - the second central moment - of the density error in each cell:

$$\mathcal{N}_{ii} = \frac{1}{N_i^2} \sum_{gal}^{N_{gal}(i)} w^2(gal). \quad (36)$$

The final aspect of the analysis is the reconstruction of the real-space density field from the redshift-space observations. This is achieved using equation 8. Following Kaiser (1987), using distant observer and small-angle approximation, the cross-correlation matrix in equation 8 for the linear regime can be written as

$$\langle s(\mathbf{r})d(\mathbf{s}) \rangle = \langle \delta_r \delta_s \rangle = \xi(r)(1 + \frac{1}{3}\beta), \quad (37)$$

where  $\mathbf{s}$  and  $\mathbf{r}$  are position vectors in redshift and real space, re-

spectively. The term,  $(1 + \frac{1}{3}\beta)$ , is easily obtained by integrating the direction dependent density field in redshift space. Using equation 37, the transformation from redshift space to real space simplifies to:

$$s^{WF}(\mathbf{r}) = \frac{1 + \frac{1}{3}\beta}{K[\beta]} \mathbf{C} [K[\beta]\mathbf{C} + \mathbf{N}]^{-1} \mathbf{d}. \quad (38)$$

As mentioned earlier, the equation above is calculated for linear scales only and hence small scale distortions (i.e. *fingers of God*) are not corrected for. For this reason, we collapse in redshift space the fingers seen in 2dF groups (Eke *et al.* 2003) with more than 75 members, 25 groups in total (11 in NGP and 14 in SGP). All the galaxies in these groups are assigned the same coordinates. As expected, correcting these small scale distortions does not change the constructed fields substantially as these distortions are practically smoothed out because of the cell size used in binning the data.

The maps shown in this section were derived by the technique detailed above. There are 80 sets of plots which show the density fields as strips in  $RA$  and  $Dec$ , 40 maps for SGP and 40 maps for NGP. Here we just show some examples, the rest of the plots can be found in url: <http://www.ast.cam.ac.uk/~pirin>. For comparison, the top plots of Figures 10, 11, 14, and 15 show the redshift space density field weighted by the selection function and the angular mask. The contours are spaced at  $\Delta\delta = 0.5$  with solid (dashed) lines denoting positive (negative) contours; the heavy solid contours correspond to  $\delta = 0$ . Also plotted for comparison are the galaxies (red dots) and the groups with  $N_{gr}$  number of members (Eke *et al.* 2003) and  $9 \leq N_{gr} \leq 17$  (green circles),  $18 \leq N_{gr} \leq 44$  (blue squares) and  $45 \leq N_{gr}$  (magenta stars). We also show the number of Abell, APM and EDCC clusters studied by De Propriis *et al.* (2002) (black upside down triangles). The middle plots show the redshift space density shown in top plots after the Wiener Filter applied. As expected, the Wiener Filter suppresses the noise. The smoothing performed by the Wiener Filter is variable and increases with distance. The bottom plots show the reconstructed real density field  $s^{WF}(\mathbf{r})$ , after correcting for the redshift distortions. Here the amplitude of density contrast is reduced slightly. We also plot the reconstructed fields in declination slices. These plots are shown in Figures 7 and 8.

We also plot the square root of the variance of the residual field (equation 2), which defines the scatter around the mean reconstructed field. We plot the residual fields corresponding to some of the redshift slices shown in this paper. (Figures 3 and 4). For better comparison, plots are made so that the cell number increases with increasing  $RA$ . If the volume of the cells used to pixelise the survey was constant, we would expect the square root of the variance  $\Delta\delta$  to increase due to the increase in shot noise (equation 7). However, since the pixelisation was constructed to keep the shot noise per pixel approximately constant,  $\Delta\delta$  also stays constant ( $\Delta\delta \approx 0.23$  for both NGP and SGP) but the average density contrast in each pixel decreases with increasing redshift. This means that although the variance of the residual in each cell is roughly equal, the relative variance (represented by  $\frac{\Delta\delta}{\delta}$ ) increases with increasing redshift. This increase is clearly evident in Figures 3 and 4. Another conclusion that can be drawn from the figures is that the bumps in the density field are due to real features not due to error in the reconstruction, even at higher redshifts.

## 6.2 Reconstruction Using Non-linear Theory

In order to increase the resolution of the density field maps, we reduce the target cell width to  $5h^{-1}$  Mpc. A volume of a cubic cell

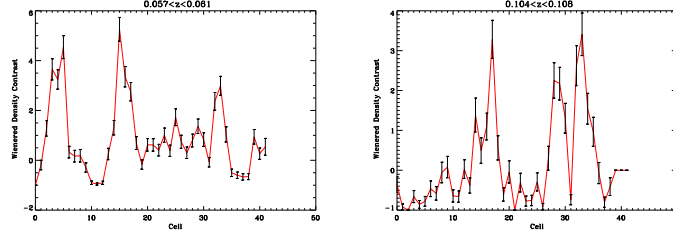


**Figure 3.** The plot of overdensities in SGP for the each redshift slice for  $10h^{-1}$  Mpc target cell size shown above. Also plotted are the variances of the residual associated for each cell. The increase in cell number indicates the increase  $RA$  in each redshift slice.

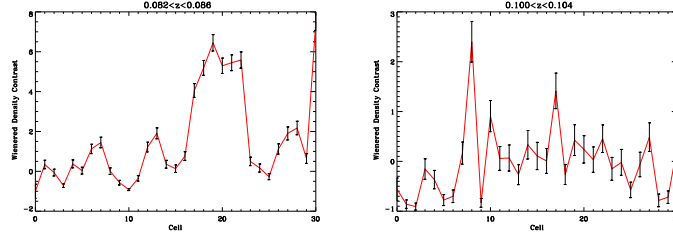


**Figure 4.** Same as in figure 3 but for the redshift slices in NGP shown above.

of side  $5h^{-1}$  Mpc is roughly equal to a top-hat sphere of radius of about  $3h^{-1}$  Mpc. The variance of the mass density field in this sphere is  $\sigma_3 \approx 1.7$  which corresponds to non-linear scales. To reconstruct the density field on these scales, we require accurate descriptions of non-linear galaxy power spectrum and the non-linear redshift space distortions.

For the non-linear matter power spectrum  $P_{\text{nl}}^R(k)$ , we adopt the empirical fitting formula of Smith *et al.* (2003). This formula, derived using the ‘halo model’ for galaxy clustering, is more accurate than the widely used Peacock & Dodds (1996) fitting formula which is based on the assumption of ‘stable clustering’ of virialized halos. We note that for the scales concerned in this paper (up to  $k \approx 10h\text{Mpc}^{-1}$ ), Smith *et al.* (2003) and Peacock & Dodds (1996) fitting formulae give very similar results. For simplicity we assume linear, scale independent biasing in order to determine the galaxy power spectrum from the mass power spectrum, where  $b$  measures the ratio between galaxy and mass distribution,

$$P_{\text{nl}}^R = b^2 P_{\text{nl}}^m, \quad (39)$$

where  $P_{\text{nl}}^R$  is the galaxy and  $P_{\text{nl}}^m$  is the matter power spectrum. We assume that  $b = 1.0$  for our analysis. While this value is in agreement with the result obtained from 2dFGRS (Lahav *et al.* 2002, Verde *et al.* 2002) for scales of tens of Mpc, it does not hold true for the scales of  $5h^{-1}$  Mpc on which different galaxy populations show different clustering patterns (Norberg *et al.* 2002, Madgwick *et al.* 2002, Zehavi *et al.* 2002). More realistic models exist where biasing is scale dependent (e.g. Seljak, 2000 and Peacock & Smith, 2000) but since the Wiener Filtering method is not sensitive to small errors in the prior parameters and the reconstruction scales are not highly non-linear, the simple assumption of no bias will still give accurate reconstructions.

The main effect of redshift distortions on non-linear scales is the reduction of power as a result of radial smearing due to virialized motions. The density profile in redshift space is then the convolution of its real space counterpart with the peculiar velocity distribution along the line of sight, leading to damping of power on small scales. This effect is known to be reasonably well approxi-

mated by treating the pairwise peculiar velocity field as Gaussian or better still as an exponential in real space (superpositions of Gaussians), with dispersion  $\sigma_p$  (e.g. Peacock & Dodds 1994, Ballinger *et al.* 1996 & Kang *et al.* 2002). Therefore the galaxy power spectrum in redshift space is written as

$$P_{\text{nl}}^S(k, \mu) = P_{\text{nl}}^R(k, \mu)(1 + \beta\mu^2)^2 D(k\sigma_p\mu), \quad (40)$$

where  $\mu$  is the cosine of the wave vector to the line of sight,  $\sigma_p$  has the unit of  $h^{-1}$  Mpc and the damping function in  $k$ -space is a Lorentzian:

$$D(k\sigma_p\mu) = \frac{1}{1 + (k^2\sigma_p^2\mu^2)/2}. \quad (41)$$

Integrating equation 40 over  $\mu$ , we obtain the direction-averaged power spectrum in redshift space:

$$\begin{aligned} \frac{P_{\text{nl}}^S(k)}{P_{\text{nl}}^R(k)} &= \frac{4(\sigma_p^2 k^2 - \beta)\beta}{\sigma_p^4 k^4} + \frac{2\beta^2}{3\sigma_p^2 k^2} \\ &+ \frac{\sqrt{2}(k^2\sigma_p^2 - 2\beta)^2 \arctan(k\sigma_p/\sqrt{2})}{k^5\sigma_p^5}. \end{aligned} \quad (42)$$

For the non-linear reconstruction, we use equation 42 instead of equation 33 when deriving the correlation function in redshift space. Figure 5 shows how the non-linear power spectrum is damped in redshift space (dashed line) and compared to the linear power spectrum (dotted line). In this plot and throughout this paper we adopt the  $\sigma_p$  value derived by Hawkins *et al.* (2002),  $\sigma_p = 506 \pm 52 \text{ km s}^{-1}$ . Interestingly, by coincidence, the non-linear and linear power spectra look very similar in redshift space. So, if we had used the linear power spectrum instead of its non-linear counterpart, we still would have obtained physically accurate reconstructions of the density field in redshift space.

The optimal density field in real space is calculated using equation 8. The cross-correlation matrix in equation 38 can now be approximated as

$$\langle \mathbf{s}(\mathbf{r}) \mathbf{d}(\mathbf{s}) \rangle = \xi(r, \mu)(1 + \beta\mu^2) \sqrt{D(k\sigma_p\mu)}. \quad (43)$$

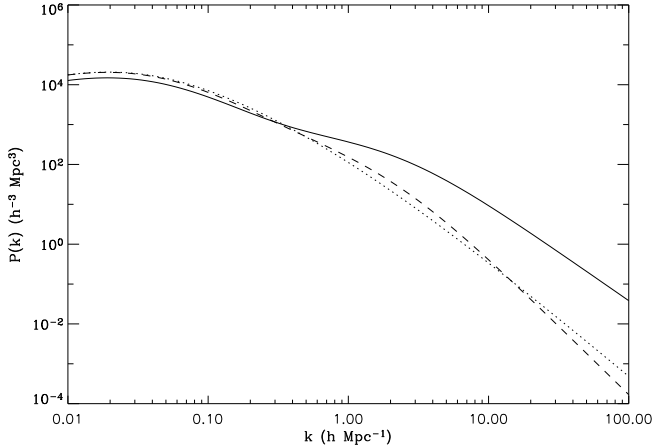


**Figure 5.** Non-linear power spectra for  $z=0$  and the concordance model with  $\sigma_p = 506 \text{ km s}^{-1}$  in real space (solid line), in redshift space from equation 42 (dashed line), both derived using the fitting formulae of Smith *et al.* (2003) and linear power spectra in redshift space derived using linear theory and Kaiser’s factor (dotted line).

Again, integrating the equation above over  $\mu$ , the direction averaged cross-correlation matrix of the density field in real space and the density field in redshift space can be written as

$$\frac{\langle \mathbf{s}(\mathbf{r}) \mathbf{d}(\mathbf{s}) \rangle}{\langle \mathbf{s}(\mathbf{r}) \mathbf{s}(\mathbf{r}) \rangle} = \frac{1}{2k^2 \sigma_p^2} \ln(k^2 \sigma_p^2 (1 + \sqrt{1 + 1/k^2 \sigma_p^2})) + \frac{\beta}{k^2 \sigma_p^2} \sqrt{1 + k^2 \sigma_p^2} + \frac{\beta}{k^3 \sigma_p^3} \text{arcsinh}(k^2 \sigma_p^2). \quad (44)$$

At the end of this paper, we show some examples of the non-linear reconstructions (Figures 9, 12, 13 and 16). As can be seen from these plots the resolution of the reconstructions improves radically, down to the scale of large clusters. Comparing Figure 15 and Figure 16 where the redshift ranges of the maps are similar, we conclude that  $10 h^{-1} \text{ Mpc}$  and  $5 h^{-1} \text{ Mpc}$  resolutions give consistent reconstructions.

Due to the very large number of cells, we reconstruct four separate density fields for redshift ranges  $0.035 \lesssim z \lesssim 0.05$  and  $0.09 \lesssim z \lesssim 0.11$  in SGP,  $0.035 \lesssim z \lesssim 0.05$  and  $0.09 \lesssim z \lesssim 0.12$  in NGP. There are 46 redshift slices in total. The number of cells for the latter reconstructions are in the order of 10 000.

To investigate the effects of using different non-linear redshift distortion approximations, we also reconstruct one field without the damping function but just collapsing the fingers of god. Although including the damping function results in a more physically accurate reconstruction of the density field in real space, it still is not enough to account for the elongation of the richest clusters along the line of sight. Collapsing the fingers of god as well as including the damping function underestimates power resulting in noisy reconstruction of the density field. We choose to use only the damping function for the non-linear scales obtaining stable results for the density field reconstruction.

The theory of gravitational instability states that as the dynamics evolve away from the linear regime, the initial field deviates from Gaussianity and skewness develops. The Wiener Filter, in the form presented here, only minimises the variance and it ignores the higher moments that describe the skewness of the underlying distribution. However, since the scales of reconstructions presented in this section are not highly non-linear and the signal-to-noise ratio

is high, the assumptions involved in this analysis are not severely violated for the non-linear reconstruction of the density field in redshift space. The real space reconstructions are more sensitive to the choice of cell size and the power spectrum since the Wiener Filter is used not only for noise suppression but also for transformation from redshift space. Therefore, reconstructions in redshift space are more reliable on these non-linear scales than those in real space.

A different approach to the non-linear density field reconstruction presented in this paper is to apply the Wiener Filter to the reconstruction of the logarithm of the density field as there is good evidence that the statistical properties of the perturbation field in the quasi-linear regime is well approximated by a log-normal distribution. A detailed analysis of the application of the Wiener Filtering technique to log-normal fields is given in Sheth (1995).

## 7 MAPPING THE LARGE SCALE STRUCTURE OF THE 2dFGRS

One of the main goals of this paper is to use the reconstructed density field to identify the major superclusters and voids in the 2dFGRS. We define superclusters (voids) as regions of large overdensity (underdensity) which is above (below) a certain threshold. This approach has been used successfully by several authors (e.g. Einasto *et al.* 2002 & 2003, Kolokotronis, Basilakos & Plionis 2002, Plionis & Basilakos 2002, Saunders *et al.* 1991).

### 7.1 The Superclusters

In order to find the superclusters listed in Table 1, we define the density contrast threshold,  $\delta_{th}$ , as distance dependent. We use a varying density threshold for two reasons that are related to the way the density field is reconstructed. Firstly, the adaptive gridding we use implies that the cells get bigger with increasing redshift. This means that the density contrast in each cell decreases. The second effect that decreases the density contrast arises due to the Wiener Filter signal tending to zero towards the edges of the survey. Therefore, for each redshift slice we find the mean and the standard deviation of the density field (averaged over 113 cells for NGP and 223 for SGP), then we calculate  $\delta_{th}$  as twice the standard deviation of the field added to its mean, averaged over SGP and NGP for each redshift bin (see Figure 6). In order to account for the clustering effects, we fit a smooth curve to  $\delta_{th}$ , using  $\chi^2$  minimisation. The best fit, also shown Figure 6, is a quadratic equation with  $\chi^2/(\text{number of degrees of freedom}) = 1.6$ . We use this fit when selecting the overdensities. We note that choosing smoothed or unsmoothed density threshold does not change the selection of the superclusters.

The list of superclusters in SGP and NGP region are given in Table 1. This table is structured as follows: column 1 is the identification, columns 2 and 3 are the minimum and the maximum redshift, columns 4 and 5 are the minimum and maximum  $RA$ , columns 6 and 7 are the minimum and maximum  $Dec$  over which the density contours above  $\delta_{th}$  extend. In column 8, we show the number of Durham groups with more than 5 members that the supercluster contains. In column 9, we show the number of Abell, APM and EDCC clusters studied by De Propris *et al.* (2002) the supercluster has. In the last column, we show the total number of groups and clusters. Note that most of the Abell clusters are counted in the Durham group catalogue. We observe that the rich groups (groups with more than 9 members) almost always reside in superclusters whereas poorer groups are more dispersed.



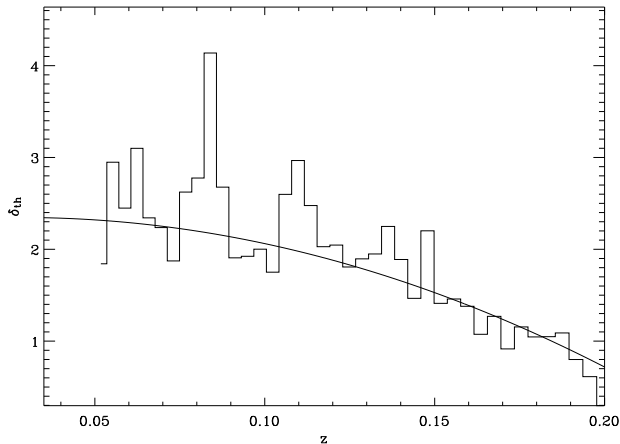


**Figure 6.** The density threshold  $\delta_{th}$  as a function of redshift  $z$  and the best fit model used to select the superclusters in Table 1.

We note that the superclusters that contain Abell clusters are on average richer than superclusters that do not contain Abell clusters, in agreement with Einasto *et al.* 2003. However, we also note that the number of Abell clusters in a rich supercluster can be equal to the number of Abell clusters in a poorer supercluster, whereas the number of Durham groups increase as the overdensity increases. Thus, we conclude that the Durham groups are in general better representatives of the underlying density distribution of 2dFGRS than Abell clusters.

The superclusters SCSGP03, SCSGP04 and SCSGP05 can be seen in Figure 10. SCSGP04 is part the rich Pisces-Cetus Supercluster which was first described by Tully (1987). SCSGP01, SCSGP02, SCSGP03 and SCSGP04 are all filamentary structures connected to each other, forming a multi branching system. SCSGP05 seems to be a more isolated system, possibly connected to SCSGP06 and SCSGP07. SCSGP06 (figure 11) is the upper part of the gigantic Horoglium Reticulum Supercluster. SCSGP07 (Figure 11) is the extended part of the Leo-Coma Supercluster. The richest supercluster in the SGP region is SCSGP16 which can be seen in the middle of the plots in Figure 12. Also shown, in the same figure, is SCSGP15, one of the richest superclusters in SGP and the edge of SCSGP17. In fact, as evident from Figure 12, SCSGP14, SCSGP15, SCSGP16 and SCSGP17 are branches of one big filamentary structure. In Figure 13, we see SCNGP01, this structure is part of the upper edge of the Shapley Supercluster. The richest supercluster in NGP is SCNGP06, shown in Figure 14. Around this, in the neighbouring redshift slices, there are two rich filamentary superclusters, SCNGP06, SCNGP08 (figure 15). SCNGP07 seems to be the node point of these filamentary structures.

Table 1 shows only the major overdensities in the survey. These tend to be filamentary structures that are mostly connected to each other.

## 7.2 The Voids

For the catalogue of the largest voids in Table 2 and Table 3, we only consider regions with 80 percent completeness or more and go up to a redshift of 0.15. Following the previous studies (e.g. El-Ad & Piran 2000, Benson *et al.* 2003 & Sheth *et al.* 2003), our chosen underdensity threshold is  $\delta_{th} = -0.85$ . The lists of galaxies and their properties that are in these voids and in the

other smaller voids that are not in Tables 2 and 3 are given in url: <http://www.ast.cam.ac.uk/~pirin>. The tables of voids is structured in a similar way as the table of superclusters, only we give separate tables for NGP and SGP voids. The most intriguing structures seen are the voids VSGP01, VSGP2, VSGP03, VSGP4 and VSGP05. These voids, clearly visible in the radial number density function of 2dFGRS, are actually part of a big superhole broken up by the low value of the void density threshold. This superhole has been observed and investigated by several authors (e.g. Cross *et al.* 2002, De Propis *et al.* 2002, Norberg *et al.* 2002, Frith *et al.* 2003). The local NGP region also has excess underdensity (VNGP01, VNGP02, VNGP03, VNGP04, VNGP05, VNGP06 and VNGP07, again part of a big superhole) but the voids in this area are not as big or as empty as the voids in local SGP. In fact, by combining the results from 2 Micron All Sky Survey, Las Campanas Survey and 2dFGRS, Frith *et al.* (2003) conclude that these underdensities suggest that there is a contiguous void stretching from north to south. If such a void does exist then it is unexpectedly large for our present understanding of large scale structure, where on large enough scales the Universe is isotropic and homogeneous.

## 8 CONCLUSIONS

In this paper we use the Wiener Filtering technique to reconstruct the density field of the 2dF galaxy redshift survey. We pixelise the survey into igloo cells bounded by  $RA$ ,  $Dec$  and redshift. The cell size varies in order to keep the number of galaxies per cell roughly constant and is approximately  $10 h^{-1}$  for Mpc high and  $5 h^{-1}$  Mpc for the low resolution maps at the median redshift of the survey. Assuming a prior based on parameters  $\Omega_m = 0.3$ ,  $\Omega_\Lambda = 0.7$ ,  $\beta = 0.49$ ,  $\sigma_8 = 0.8$  and  $\Gamma = 0.2$ , we find that the reconstructed density field clearly picks out the groups catalogue built by Eke *et al.* (2003) and Abell, APM and EDCC clusters investigated by De Propis *et al.* (2002). We also reconstruct four separate density fields with different redshift ranges for a smaller cell size of  $5 h^{-1}$  Mpc at the median redshift. For these reconstructions, we assume a non-linear power spectrum fit developed by Smith *et al.* (2003) and linear biasing. The resolution of the density field improves dramatically, down to the size of big clusters. The derived high resolution density fields is in agreement with the lower resolution versions.

We use the reconstructed fields to identify the major superclusters and voids in SGP and NGP. We find that the richest superclusters are filamentary and multi branching, in agreement with Einasto *et al.* 2002. We also find that the rich clusters always reside in superclusters whereas poor clusters are more dispersed. We present the major superclusters in 2dFGRS in Table 1. We pick out two very rich superclusters, one in SGP and one in NGP. We also identify voids as underdensities that are below  $\delta \approx -0.85$  and that lie in regions with more that 80% completeness. These underdensities are presented in Table 2 (SGP) and Table 3 (NGP). We pick out two big voids, one in SGP and one in NGP. Unfortunately, we cannot measure the sizes and masses of the large structures we observe in 2dF as most of these structures continue beyond the boundaries of the survey.

The detailed maps and lists of all of the reconstructed density fields, plots of the residual fields and the lists of the galaxies that are in underdense regions can be found on WWW at <http://www.ast.cam.ac.uk/~pirin>.

One of the main aims of this paper is to identify the large scale structure in 2dFGRS. The Wiener Filtering technique provides a rigorous methodology for variable smoothing and noise

suppression. As such, a natural continuation of this work is using the Wiener filtering method in conjunction with other methods to further investigate the geometry and the topology of the supercluster-void network. Sheth *et al.* (2003) developed a powerful surface modelling scheme, SURFGEN, in order to calculate the Minkowski Functionals of the surface generated from the density field. The four Minkowski functionals – the area, the volume, the extrinsic curvature and the genus – contain information about the geometry, connectivity and topology of the surface (cf. Mecke, Buchert & Wagner 1994 and Sheth *et al.* 2003) and thus they will provide a detailed morphological analysis of the superclusters and voids in 2dFGRS.

Although not applicable to 2dFGRS, the Wiener reconstruction technique is well suited to recovering the velocity fields from peculiar velocity catalogues. Comparisons of galaxy density and velocity fields allow direct estimations of the cosmological parameters such as the bias parameter and the mean mass density. These comparisons will be possible with the upcoming 6dF Galaxy Survey (<http://www.mso.anu.edu.au/6dFGS>) which will measure the redshifts of 170,000 galaxies and the peculiar velocities of 15,000 galaxies by June 2005. Compared to 2dFGRS, the 6dF survey has a much higher sky-coverage (the entire southern sky down to  $|b| > 10^\circ$ ). This wide survey area would allow a full hemispheric Wiener reconstruction of large scale structure so that the sizes and masses of the superclusters and voids can be determined.

## ACKNOWLEDGEMENTS

The 2dF Galaxy Redshift Survey was made possible through the dedicated efforts of the staff at Anglo-Australian Observatory, both in crediting the two-degree field instrument and supporting it on the telescope. PE acknowledges support from the Middle East Technical University, Ankara, Turkey, the Turkish Higher Education Council and Overseas Research Trust. This research was conducted utilising the super computer COSMOS at DAMTP, Cambridge.

## REFERENCES

- Ballinger W.E., Peacock J.A. & Heavens A.F., 1996, MNRAS, 282, 877  
 Benson A., Hoyle F., Torres F., Vogeley M., 2003, MNRAS, 340, 160  
 Bond J.R., Kofman L., Pogosyan D., 1996, Nature, 380, 603  
 Bouchet F.R., Gispert R., Phys. Rev. Lett., 74, 4369  
 Bunn E., Fisher K.B., Hoffman Y., Lahav O., Silk J., Zaroubi S., 1994, ApJ, 432, L75  
 Cross M., and 2dFGRS team, 2001, MNRAS, 324, 825  
 Colles M., and 2dFGRS team, 2001, MNRAS, 328, 1039  
 Davis M., Huchra J.P., 1982, ApJ, 254, 437  
 Davis M., Geller M.J., 1976, ApJ, 208, 13  
 De Propriis R. & the 2dFGRS team, 2002, MNRAS, 329, 87  
 Dressler A., 1980, ApJ, 236, 351.  
 El-Ad H., Piran T., 2000, MNRAS, 313, 553  
 Einasto J., Htsi G., Einasto G., Saar E., Tucker D.L., Mller V., Heinmki P., Allam S.S. 2002, astro-ph/02123112  
 Einasto J., Einasto G., Htsi G., Saar E., Tucker D.L., Tago E., Mller V., Heinmki P., Allam S.S. 2003, astro-ph/0304546  
 Eisenstein D.J., Hu W., 1998, ApJ, 518, 2  
 Efstathiou G., Moody S., 2001, MNRAS, 325, 1603  
 Eke V., & 2dFGRS Team, 2003, submitted to MNRAS  
 Frith W.J., Busswell G.S., Fong R., Metcalfe N., Shanks T., 2003, submitted to MNRAS  
 Fisher K.B., Lahav O., Hoffman, Y., Lynden-Bell and Zaroubi S., 1995, MNRAS, 272, 885  
 Freedman W.L., 2001, ApJ, 553, 47  
 Hawkins E., & the 2dFGRS team, 2002, MNRAS, in press.  
 Hogg D.W. *et al.*, 2003, ApJ, 585, L5  
 Kaiser N., 1987, MNRAS, 227, 1  
 Kang X., Jing Y.P., Mo H.J., Brner G., 2002, MNRAS, 336, 892  
 Kolokotronis V., Basilakos S. & Plionis M., 2002, MNRAS, 331, 1020.  
 Lahav O., Fisher, K.B., Hoffman, Y., Scharf, C.A. and Zaroubi, S., Wiener Reconstruction of Galaxy Surveys in Spherical Harmonics, 1994, The Astrophysical Journal Letters, 423, L93  
 Lahav O. & the 2dFGRS team, 2002, MNRAS, 333, 961.  
 Maddox S.J., Efstathiou G., Sutherland W.J., 1990, MNRAS, 246, 433.  
 Maddox, S.J., 2003, in preparation.  
 Madgwick D. and 2dFGRS team, 2002, 333,133  
 Madgwick D. and 2dFGRS team, 2003, MNRAS, 344, 847  
 Mecke K.R., Buchert T. & Wagner, 1994, A&A, 288, 697  
 Moody S., PhD Thesis, 2003  
 Nusser A. & Davis M., 1994, ApJ, 421, L1  
 Norberg P. and 2dFGRS team, 2001, MNRAS, 328, 64  
 Norberg P. and 2dFGRS team, 2002, MNRAS, 332, 827  
 Peacock J.A. & Dodds S.J., 1994, MNRAS, 267, 1020  
 Peacock J.A. & Dodds S.J., 1996, MNRAS, 280, L19  
 Peacock J.A. & Smith R.E., 2000, MNRAS, 318, 1144  
 Peacock J.A. & the 2dFGRS team, 2001, Nature, 410, 169  
 Percival W. & the 2dFGRS team, 2001, MNRAS, 327, 1297  
 Plionis M., Basilakos S., 2002, MNRAS, 330, 339.  
 Press W.H., Vetterling W.T., Teukolsky S.A., Flannery B. P., 1992, Numerical Recipes in Fortran 77, 2nd edn., Cambridge University Press, Cambridge  
 Rybicki, G.B & Press, W.H., 1992, ApJ, 398, 169.  
 Saunders W., Frenk C., Rowan-Robinson M., Lawrence A., Efstathiou G., 1991, Nature, 349, 32  
 Scharf C.A., Hoffman Y., Lahav O., Lyden-Bell D, 1992, MNRAS, 264, 439.  
 Schmoltdt I.M. *et al.*, 1999, ApJ, 118, 1146  
 Sheth J.V., Sahni V., Shandarin S.F., Sathyaprakah B.S., 2003, MNRAS, in press.  
 Seljak U., 2000, MNRAS, 318, 119  
 Sheth J.V., 2003, submitted to MNRAS  
 Sheth R.K., 1995, MNRAS, 264, 439  
 Smith R.E. *et al.*, 2003, MNRAS, 341, 1311  
 Tegmark M., Efstathiou G., 1996, MNRAS, 281, 1297.  
 Tully B., 1987, *Atlas of Nearby Galaxies*, Cambridge University Press  
 Wiener N., 1949, in *Extrapolation and Smoothing of Stationary Time Series*, (New York: Wiley)  
 Yahil A., Strauss M.A. & Huchra J.P., 1991, ApJ, 372, 380  
 Zaroubi S., Hoffman, Y., Fisher, K., and Lahav, O., Wiener Reconstruction of the Large Scale Structure, 1995, The Astrophysical Journal, 449, 446.  
 Zaroubi S., Hoffman, Y., 1996, ApJ, 462, 25.  
 Zaroubi S., 2002, MNRAS, 331, 901  
 Zehavi I. & the SDSS collaboration, 2002, ApJ., 501, 172

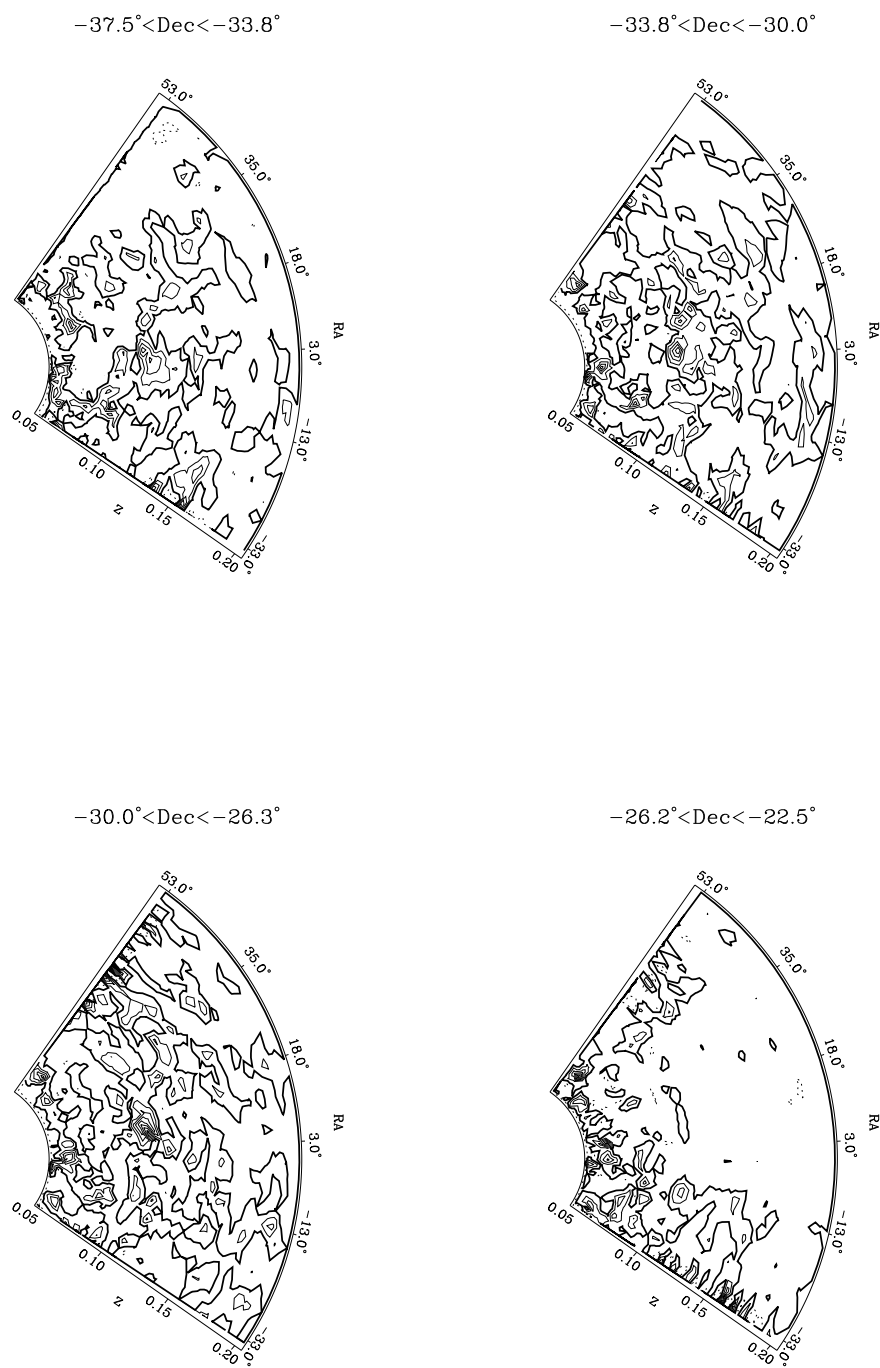


**Figure 7.** Reconstructions of the 2dFGRS SGP region in slices of declination for  $10h^{-1}$  Mpc target cell size . The declination range is given on top each plot. The contours are spaced at  $\Delta\delta = 1.0$  with solid (dashed) lines denoting positive (negative) contours; the heavy solid contours correspond to  $\delta = 0$

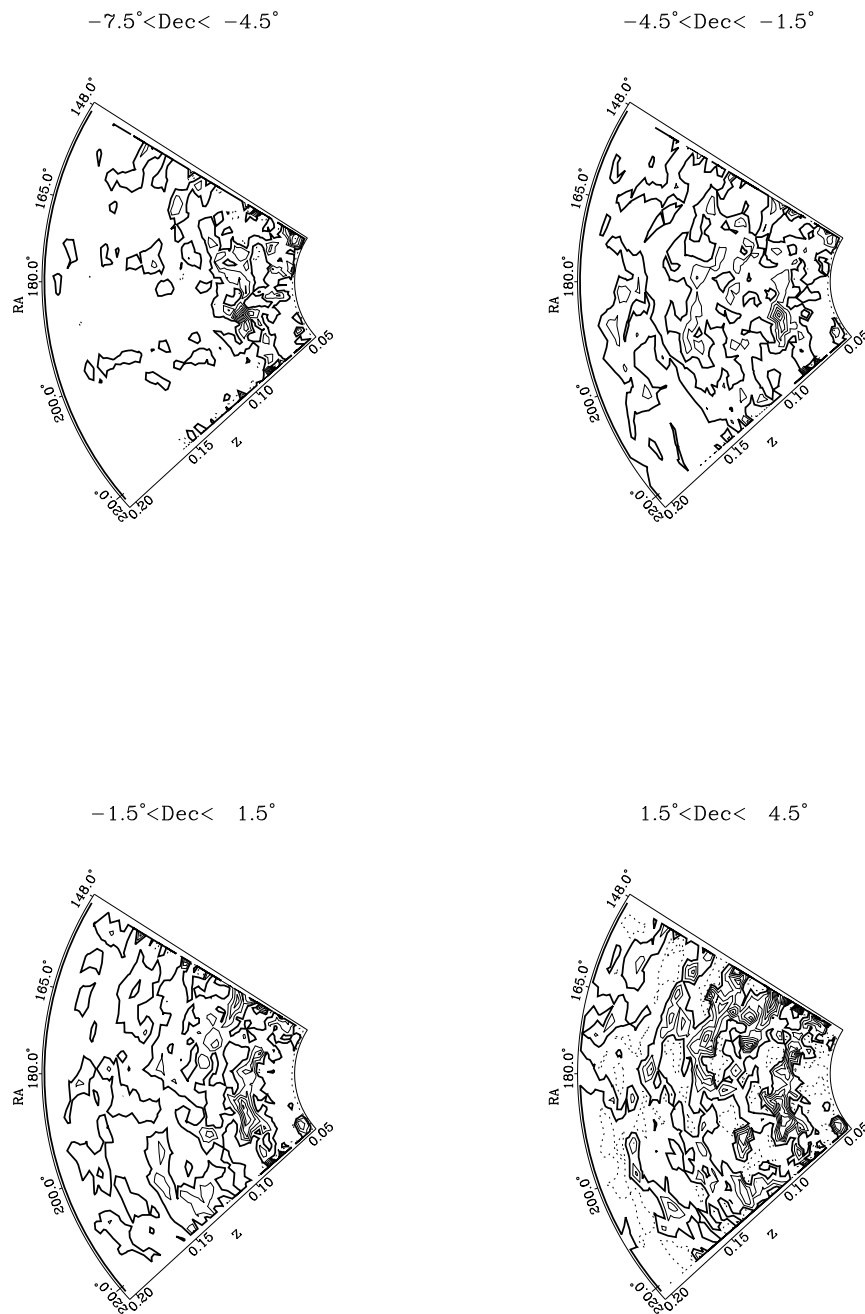


**Figure 8.** Reconstructions of the 2dFGRS NGP region in slices of declination for  $10h^{-1}$  Mpc target cell size. The declination range is given on top each plot. The contours are spaced at  $\Delta\delta = 1.0$  with solid (dashed) lines denoting positive (negative) contours; the heavy solid contours correspond to  $\delta = 0$

**Figure 9.** Reconstructions of the 2dFGRS SGP region for the redshift range:  $0.047 \leq z \leq 0.049$  for  $5h^{-1}$  Mpc target cell size. The contours are spaced at  $\Delta\delta = 0.5$  with solid (dashed) lines denoting positive (negative) contours; the heavy solid contours correspond to  $\delta = 0$ . The red dots denote the galaxies with redshifts in the plotted range. a) Redshift space density field weighted by the selection function and the angular mask. b) Same as in a) but smoothed by a Wiener Filter c) Same as in b) but corrected for the redshift distortion. The overdensity centred on: 1)  $RA \approx -23.5$ ,  $Dec \approx -30.0$  is SCSGP03 (see Table 1); 2)  $RA \approx 0.0$ ,  $Dec \approx -30.0$  is SCSGP04; 3)  $RA \approx 36.0$ ,  $Dec \approx -29.3$  is SCSGP05. The underdensity centred on  $RA \approx -20.5$ ,  $Dec \approx -30.0$  is VSGP01; 2)  $RA \approx -8.5$ ,  $Dec \approx -29.3$  is VSGP02; 3)  $RA \approx 18.0$ ,  $Dec \approx -28.5$  is VSGP04; 4)  $RA \approx 32.2$ ,  $Dec \approx -29.5$  is VSGP05. (see Table 2).

**Figure 10.** Reconstructions of the 2dFGRS SGP region for the redshift range:  $0.057 \leq z \leq 0.061$  for  $10h^{-1}$  Mpc target cell size. Same as in figure 9. The overdensity centred on: 1)  $RA \approx -23.5$ ,  $Dec \approx -30.0$  is SCSGP03 (see Table 1); 2)  $RA \approx 0.0$ ,  $Dec \approx -30.0$  is SCSGP04, this overdensity is part of the Pisces-Cetus Supercluster; 3)  $RA \approx 36.0$ ,  $Dec \approx -29.3$  is SCSGP05. The underdensity centred on  $RA \approx -10.0$ ,  $Dec \approx -30.0$  is VSGP12 (see Table 2).

**Figure 11.** Reconstructions of the 2dFGRS SGP region for the redshift range:  $0.068 \leq z \leq 0.071$  for  $10h^{-1}$  Mpc target cell size. Same as in figure 9. The overdensity centred on: 1)  $RA \approx 39.0$ ,  $Dec \approx -34.5$  is SCSGP07 (see Table 1) and is part of Leo-Coma Supercluster; 2)  $RA \approx 0.0$ ,  $Dec \approx -30.0$  is SCSGP06 and is part of Horoglium Reticulum Supercluster; (see Table 1).

**Figure 12.** Reconstructions of the 2dFGRS SGP region for the redshift range:  $0.107 \leq z \leq 0.108$  for  $5h^{-1}$  Mpc target cell size. Same as in figure 9. The overdensity centred on: 1)  $RA \approx 1.7$ ,  $Dec \approx -31.0$  is SCSGP16 (see Table 1); 2)  $RA \approx 36.3$ ,  $Dec \approx -30.0$  is SCSGP15. 3)  $RA \approx -15.0$ ,  $Dec \approx -30.0$  is SCSGP17. The underdensity centred on: 1)  $RA \approx -25.0$ ,  $Dec \approx -35.2$  is VSGP25 (see Table 2); 2)  $RA \approx 11.3$ ,  $Dec \approx -24.5$  is VSGP22; 3)  $RA \approx 48.0$ ,  $Dec \approx -30.5$  is VSGP20.

**Figure 13.** Reconstructions of the 2dFGRS NGP region for the redshift range:  $0.039 \leq z \leq 0.041$  for  $5h^{-1}$  Mpc target cell size. Same as in figure 9. The overdensity centred on  $RA \approx 153.0$ ,  $Dec \approx -4.0$  is SCNGP01 and is part of the Shapley Supercluster (see Table 1). The underdensities are VNGP01, VNGP02, VNGP03, VNGP04, VNGP05, VNGP06 and VNGP07 (see Table 3)

**Figure 14.** Reconstructions of the 2dFGRS NGP region for the redshift range:  $0.082 \leq z \leq 0.086$  for  $10h^{-1}$  Mpc target cell size. Same as in figure 9. The overdensity centred on  $RA \approx 194.0$ ,  $Dec \approx -2.5$  is SCNGP06 (see Table 1).

**Figure 15.** Reconstructions of the 2dFGRS NGP region for the redshift range:  $0.100 \leq z \leq 0.104$  for  $10h^{-1}$  Mpc target cell size. Same as in figure 9. The overdensity centred on: 1)  $RA \approx 170.0$ ,  $Dec \approx -1.0$  is SCNGP08 (see Table 1). The underdensity centred on: 1)  $RA \approx 150.0$ ,  $Dec \approx -1.5$  is VNGP18 (see Table 3); 2)  $RA \approx 192.5$ ,  $Dec \approx 0.5$  is VNGP19; 2)  $RA \approx 209.0$ ,  $Dec \approx -1.5$  is VNGP17.

**Figure 16.** Reconstructions of the 2dFGRS NGP region for the redshift range:  $0.103 \leq z \leq 0.108$  for  $5h^{-1}$  Mpc target cell size. Same as in figure 9.

**Table 1.** The list of superclusters

<i>No</i>	$z_{min}$	$z_{max}$	$RA_{min}$ (1950) deg	$RA_{max}$ (1950) deg	$Dec_{min}$ (1950) deg	$Dec_{max}$ (1950) deg	$N_{gr} \geq 9$	$N_{clus}$	$N_{total}$
SCSGP01	0.048	0.054	-11.5	-3.2	-37.5	-25.5	23	9	27
SCSGP02	0.054	0.057	-22.3	0.0	-35.5	-33.0	9	1	9
SCSGP03	0.057	0.064	-29.4	-17.5	-37.5	-22.5	23	8	26
SCSGP04	0.057	0.068	-10.0	+10.0	-35.5	-24.0	34	14	37
SCSGP05	0.054	0.064	32.5	39.0	-33.0	-25.5	14	7	18
SCSGP06	0.064	0.082	45.5	55.0	-35.0	-24.0	26	7	31
SCSGP07	0.064	0.071	18.5	40.0	-35.0	-31.0	10	4	11
SCSGP08	0.068	0.075	-38.5	-33.0	-35.0	-22.5	9	3	11
SCSGP09	0.075	0.082	-27.0	-17.5	-37.5	-22.5	20	9	24
SCSGP10	0.082	0.093	-17.5	-9.5	-36.0	-29.0	18	9	21
SCSGP11	0.086	0.097	-33.0	-27.0	-34.5	-24.0	14	4	15
SCSGP12	0.093	0.097	-22.0	-17.4	-36.0	-34.8	4	1	5
SCSGP13	0.093	0.097	0.0	3.8	-36.0	-34.8	3	0	3
SCSGP14	0.093	0.104	16.0	24.6	-33.0	-28.2	8	1	8
SCSGP15	0.097	0.115	28.0	44.6	-35.2	-24.6	34	18	41
SCSGP16	0.100	0.119	1.5	21.9	-35.2	-26.5	93	20	98
SCSGP17	0.100	0.108	-27.1	-3.0	-35.2	-26.5	38	7	43
SCSGP18	0.150	0.166	1.5	31.8	-33.0	-26.5	18	6	22
SCSGP19	0.162	0.177	22.8	34.5	-35.2	-24.6	13	5	15
SCSGP20	0.181	0.202	-17.5	-3.15	-35.5	-24.6	13	4	14
SCNGP01	0.035	0.068	147.5	174.5	-6.5	2.5	59	6	61
SCNGP02	0.048	0.061	210.0	218.5	-5.0	0.0	19	0	19
SCNGP03	0.068	0.075	150.0	155.0	-1.0	2.5	6	0	6
SCNGP04	0.068	0.075	158.0	166.5	-1.0	2.5	8	1	9
SCNGP05	0.071	0.082	171.0	184.0	-3.5	2.5	27	6	28
SCNGP06	0.079	0.094	185.0	202.5	-7.5	2.5	77	7	79
SCNGP07	0.086	0.101	147.0	181.5	-5.5	2.5	31	4	34
SCNGP08	0.090	0.131	165.0	185.0	-6.3	2.5	51	10	57
SCNGP09	0.103	0.114	158.5	163.0	-1.3	2.5	8	1	9
SCNGP10	0.103	0.118	197.0	203.0	-3.75	1.25	22	0	22
SCNGP11	0.123	0.131	147.0	173.0	0.0	2.5	3	2	3
SCNGP12	0.119	0.142	210.0	219.0	-4.0	1.3	19	2	20
SCNGP13	0.131	0.142	173.0	179.0	-6.25	-1.3	5	2	6
SCNGP14	0.131	0.142	185.0	193.0	-6.25	1.3	7	0	7
SCNGP15	0.131	0.138	155.0	160.0	-6.3	1.3	9	1	9
SCNGP16	0.142	0.146	166.0	174.0	-0.3	1.3	5	0	5
SCNGP17	0.142	0.146	194.0	199.0	-2.5	1.3	1	0	1
SCNGP18	0.146	0.150	204.0	210.0	-2.5	1.3	4	0	4
SCNGP19	0.173	0.177	181.0	184.0	-1.0	-4.0	3	0	3
SCNGP20	0.181	0.185	185.5	193.0	-1.0	-4.0	1	0	1

Table 2. The list of voids in SGP

<i>No</i>	$z_{min}$	$z_{max}$	$RA_{min}$ (1950) deg	$RA_{max}$ (1950) deg	$Dec_{min}$ (1950) deg	$Dec_{max}$ (1950) deg
VSGP01	0.035	0.051	-27.5	-17.3	-37.5	-22.5
VSGP02	0.035	0.051	-17.3	0.0	-33.0	-25.5
VSGP03	0.035	0.048	0.9	11.5	-34.5	-28.5
VSGP04	0.035	0.051	12.4	23.6	-30.5	-26.0
VSGP05	0.035	0.054	23.6	40.8	-33.5	-26.0
VSGP06	0.035	0.042	32.8	37.3	-33.5	-28.5
VSGP07	0.035	0.051	39.5	46.4	-31.5	-28.5
VSGP08	0.035	0.042	46.4	51.0	-31.5	-28.5
VSGP09	0.039	0.044	-35.5	-30.0	-34.5	-28.5
VSGP10	0.039	0.041	10.0	17.5	-33.5	-29.5
VSGP11	0.041	0.044	15.5	22.5	-33.5	-28.5
VSGP12	0.057	0.061	-12.8	-8.2	-31.5	-28.5
VSGP13	0.082	0.086	5.4	8.0	-31.5	-28.5
VSGP15	0.082	0.089	41.8	49.3	-31.5	-28.5
VSGP16	0.086	0.089	12.5	16.3	-31.5	-28.5
VSGP17	0.086	0.089	31.0	33.5	-32.5	-28.5
VSGP18	0.089	0.097	-8.2	-5.95	-30.5	-29.5
VSGP19	0.089	0.093	42.7	45.5	-30.5	-29.5
VSGP20	0.093	0.104	46.4	52.5	-32.5	-28.2
VSGP21	0.093	0.100	28.2	32.8	-31.5	-28.5
VSGP22	0.097	0.104	7.7	12.5	-32.0	-28.5
VSGP23	0.097	0.100	-12.8	-11.5	-32.0	-28.5
VSGP24	0.100	0.108	-31.8	-25.3	-28.5	-25.5
VSGP25	0.100	0.112	-25.3	-21.9	-34.5	-33.0
VSGP26	0.112	0.119	-7.0	-3.7	-31.5	-28.5
VSGP27	0.112	0.115	1.5	5.4	-30.0	-27.0
VSGP28	0.112	0.115	25.9	28.2	-30.0	-27.0
VSGP29	0.112	0.115	41.0	46.4	-30.0	-27.0
VSGP30	0.115	0.119	26.2	30.5	-34.5	-31.5
VSGP31	0.119	0.123	-35.0	-30.8	-28.5	-25.5
VSGP32	0.119	0.123	-27.0	-25.5	-28.5	-26.5
VSGP33	0.119	0.123	-12.8	-10.0	-28.5	-25.5
VSGP34	0.119	0.123	41.5	49.3	-38.8	-31.8
VSGP35	0.119	0.127	11.2	16.5	-28.2	-27.5
VSGP36	0.123	0.131	-26.4	-22.4	-31.5	-28.5
VSGP37	0.123	0.127	-12.8	-8.2	-30.0	-27.0
VSGP38	0.131	0.142	-26.4	-19.5	-34.5	-31.5
VSGP39	0.131	0.138	32.3	37.5	-35.2	-24.8
VSGP40	0.138	0.142	30.3	33.5	-33.5	-29.0

**Table 3.** The list of voids in NGP

<i>No</i>	$z_{min}$	$z_{max}$	$RA_{min}$ (1950) deg	$RA_{max}$ (1950) deg	$Dec_{min}$ (1950) deg	$Dec_{max}$ (1950) deg
VNGP01	0.035	0.054	147.0	160.0	−4.0	1.5
VNGP02	0.035	0.041	166.0	171.0	−1.0	2.5
VNGP03	0.035	0.046	171.0	181.2	−1.5	2.5
VNGP04	0.035	0.051	183.0	189.0	−1.5	2.5
VNGP05	0.035	0.046	189.0	197.0	−1.5	2.0
VNGP06	0.035	0.046	202.2	206.0	−1.5	2.0
VNGP07	0.037	0.046	204.2	215.6	−2.0	0.0
VNGP08	0.041	0.051	163.8	169.8	−4.5	2.5
VNGP09	0.049	0.061	177.0	196.4	−3.5	2.5
VNGP10	0.054	0.057	165.5	173.0	−1.5	2.5
VNGP11	0.057	0.061	163.5	166.0	0.0	1.5
VNGP12	0.054	0.061	206.0	208.0	−1.5	0.5
VNGP13	0.071	0.075	176.0	179.0	−1.0	0.5
VNGP14	0.079	0.094	186.5	204.2	−7.5	0.5
VNGP15	0.092	0.097	150.8	160.2	−7.5	−6.0
VNGP16	0.093	0.100	147.0	149.5	−6	1.5
VNGP17	0.094	0.101	204.0	211.5	−3.5	2.5
VNGP18	0.099	0.115	147.5	153.6	−4.0	1.0
VNGP19	0.099	0.120	188.8	197.0	−3.0	2.5
VNGP20	0.112	0.120	176.6	178.0	0.5	2.5
VNGP21	0.110	0.115	211.6	217.0	−2.5	−0.5
VNGP22	0.110	0.123	200.2	205.0	−3.25	2.5
VNGP23	0.123	0.131	169.0	174.0	−4.0	−1.25
VNGP24	0.127	0.131	182.5	188.0	0.0	2.5
VNGP25	0.127	0.131	197.5	202.0	−1.25	0.5
VNGP26	0.134	0.142	179.5	187.5	−2.0	2.5
VNGP27	0.134	0.138	204.0	207.0	−1.5	0.0
VNGP28	0.138	0.150	147.0	154.6	−3.5	2.5
VNGP29	0.142	0.150	162.0	166.0	−4.0	1.5
VNGP30	0.142	0.150	172.6	178.0	−1.0	2.5